Nuclear Inst. and Methods in Physics Research, A 1012 (2021) 165224

Contents lists available at ScienceDirect

Nuclear Inst. and Methods in Physics Research, A

journal homepage: www.elsevier.com/locate/nima

Fast-neutron response of the novel scintillator caesium hafnium chloride

M.P. Taggart [a], J. Henderson [a], J. O'Neill [a], R. Hawrami [b], E. Ariesanti [b], A. Burger [b], P.J. Sellin [a,*]

[a] Department of Physics, University of Surrey, Guildford, Surrey, UK
[b] Fisk University, 1000 Seventeenth Ave., Nashville, TN 37208, USA

ARTICLE INFO

Keywords:
Neutron detection
Silicon photomultiplier

ABSTRACT

This paper reports on the performance of the inorganic scintillator caesium hafnium chloride (CHC) under exposure to the mixed radiation field of an AmBe neutron source and coupled to a silicon photomultiplier (SiPM). The neutron response is determined using the pulse shape discrimination charge comparison technique which can clearly identify both the (n,α) and (c) reactions in the material. Figures of merit for the pulse shape discrimination are presented and the quenching of the different channels is assessed through comparison to Monte Carlo simulations.

1. Introduction

Dual-mode neutron-γ detectors are those capable of the simultaneous measurement of both neutron and γ-ray radiation. Such detectors (typically scintillators) have come to prominence in recent years with the development of Cs_2LiYCl_6 (CLYC) [1–4] and a number of related materials (e.g. Refs. [5,6]). In CLYC, two isotopes provide the primary neutron-detection capability, ^{6}Li and ^{35}Cl. In a previous work [7], we demonstrated that the widely-used lanthanum-halide scintillator $LaCl_3$ exhibited a fast neutron response due to the presence of ^{35}Cl. Here, we investigate the novel scintillator Cs_2HfCl_6 and demonstrate that it too exhibits fast-neutron detection capabilities and makes an intriguing candidate for fast-neutron measurements.

Cs_2HfCl_6 (henceforth CHC) [8,9] has a number of properties that make it a potentially promising dual-mode scintillation material. Firstly, its effective Z and density (Z_{eff} = 58, ρ = 3.86 g/cm^3) make it well suited for detecting γ rays, even at high energies. From the perspective of neutron detection it only has one significant neutron-interacting isotope (^{35}Cl). By comparison as previously mentioned, CLYC contains both ^{35}Cl and ^{6}Li, resulting in a more complicated response. This is especially problematic for the ^{35}Cl(n,α) channel which becomes significant for higher energy neutrons as seen in Fig. 1 and is typically contaminated by the ^{6}Li(n,t) reaction which also produces α-particles. This can be overcome in CLYC by depleting the ^{6}Li content (e.g. Ref. [10]), although even a small ^{6}Li remnant can prove problematic due to the large cross section for the ^{6}Li(n,t) reaction, especially with thermal neutrons. In comparison with $LaCl_3$ (which might seem the most directly comparable material), CHC contains no significant naturally occurring radioactive contaminants whereas, in common with all lanthanum halides, actinium contamination in $LaCl_3$ is presently unavoidable. As seen in our previous work [7], this naturally occurring contamination directly interferes with the ^{35}Cl(n,α) channel. In the absence of this contamination, CHC might give full access to both the ^{35}Cl(n,p) and ^{35}Cl(n,α) channels, important for disentangling the full incident neutron spectrum.

2. Experimental technique

A sample of CHC was produced at Fisk University using the Bridgman technique [8,11]. The crystal was grown to a size of 17 × 19 × 9 mm and polished under mineral oil to produce an optical finish. Further details of CHC material processing and growth can be found in Ref. [12].

2.1. Internal radiation

The intrinsic background of the CHC scintillator was assessed through the use of a low-background hyper-pure germanium (HPGe) detector. The detector was surrounded by a 5 cm thick lead shield with an additional layer of copper to reduce the characteristic 74 keV Pb X-ray. The data acquisition chain comprises a Canberra 3106D PSU, an Ortec 570 shaping amplifier, and an Ortec EasyMCA, processed by the Ortec Maestro software.

Measurements were taken of both the room and scintillator intrinsic backgrounds for a duration of 7 days (604 800 s live time) and are shown as Fig. 2. There is no internal γ radioactivity detected by the HPGe, with the strong lines shown in Fig. 2 present in both datasets and indicative of room background.

* Corresponding author.
E-mail address: p.sellin@surrey.ac.uk (P.J. Sellin).

https://doi.org/10.1016/j.nima.2021.165224
Received 11 November 2020; Received in revised form 19 February 2021; Accepted 3 March 2021
Available online 13 March 2021

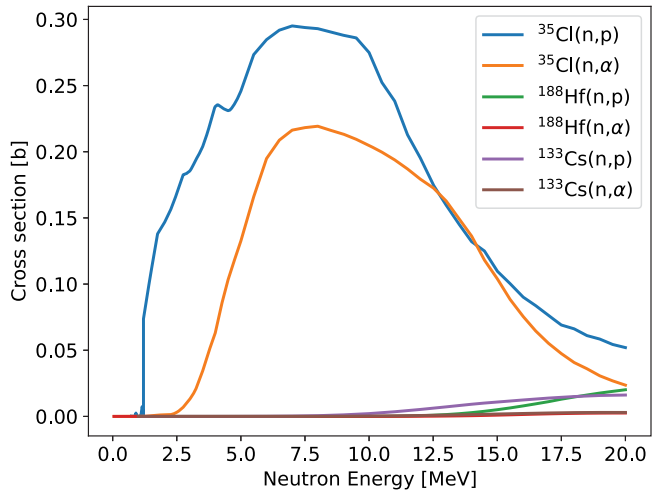

Fig. 1. Proton and α-particle producing cross sections for the most abundant chlorine, hafnium and caesium isotopes. Clearly the ^{35}Cl(n,p) and ^{35}Cl(n,α) cross sections are the most relevant for incident neutron energies between about 1 MeV and 20 MeV. Cross sections taken from the ENDF VIII evaluation [13].

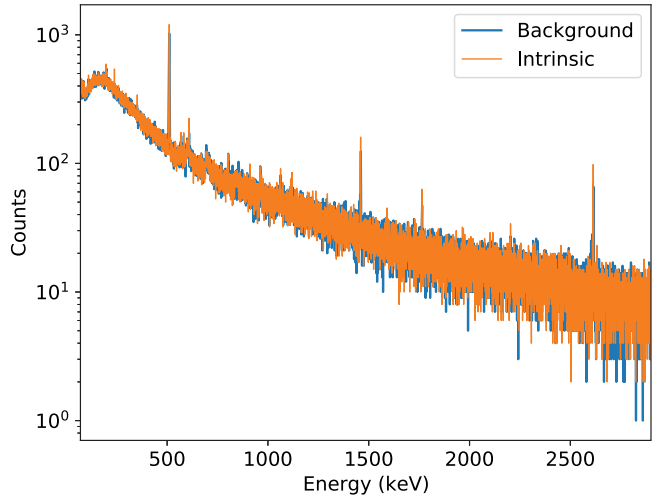

Fig. 2. Intrinsic radiation of the Cs_2HfCl_6 crystal as measured with a seven day exposure to a HPGe detector and compared to a background measurement. No excess events are seen above background, indicating no significant sources of intrinsic γ-ray producing radiation.

2.2. Detector fabrication and data acquisition

The CHC scintillator was attached to a 2 × 2 array of SensL 6 mm J-series silicon photomultipliers (SiPM) with the 17 mm × 19 mm face coupled via a thin layer of Dow Corning silicon high vacuum grease. This setup has had previous good results for neutron-γ discrimination measurements which have been published [7,14] and takes advantage of the SiPM's low power consumption and small form-factor. The scintillator was wrapped with 8 layers of 0.075 mm thick PTFE tape to improve light collection. We have previously established that beyond this level of wrapping diminishing returns begin to set in. The entire detector is housed within a light-tight aluminium enclosure.

The SiPMs are powered via a CAEN N1419 PSU with an overvoltage of 2.5 V (27.3 V operating voltage) with a summed output of all four SiPMs fed into a fast digitiser. The digitiser selected was the Caen V1730C, which has an ADC resolution of 14-bits, a dynamic range set to 0.5 V, a sampling rate of 500 MS/s, and a bandwidth of 250 MHz. The full waveform of each pulse was captured for offline processing using an analysis code written in the ROOT [15] framework that has previously been used for similar studies.

2.3. Pulse shape discrimination

The technique of pulse shape discrimination is widely known and has seen extensive use in many fields. It can, however, take a variety of forms so we shall briefly describe the method used here. The charge comparison method is a simple technique whereby two gates are applied over the pulse and a PSD parameter is calculated as:

$$PSD = 1 - \frac{Q_s}{Q_l}. \quad (1)$$

where, Q_s, is the charge integrated within the short gate, and, Q_l, the charge within the long gate, in this case the entire duration of the pulse. During this work the optimal short gate setting was established to be 2 μs encompassing the peak and early part of the pulse.

2.4. Neutron measurement

This work follows the methodology used in Ref. [7]. The CHC crystal was exposed to an AmBe source without ("fast") and with ("thermal") water moderation. The exposures were of the same duration, and a background measurement of the same duration was also performed. Fig. 3 shows the PSD parameter plotted against the γ-ray calibrated energy for the three measurements.

Fig. 3 shows the difference in detector response to high- (fast) and low-energy (thermal) neutrons compared to the background. Two additional reaction channels emerge with exposure to fast neutrons as a lower-PSD shoulder to the γ ray distribution and a new low-PSD locus, corresponding (as in Ref. [7]) to the ^{35}Cl(n,p) and ^{35}Cl(n,α) reactions respectively. As seen in Fig. 1 these reactions have approximate neutron-energy thresholds of 1 MeV and 3 MeV, respectively. Also shown in Fig. 3 are projections along the PSD axis. We note a low level of α-like events in the background spectrum, perhaps indicative of α-emitting radioactive contaminants at a very low level. This background is many orders of magnitude weaker than was seen in lanthanum halide detectors [7] however, and does not significantly interfere with a fast-neutron analysis.

By projecting along the PSD axis and fitting the resultant histogram with three normal distributions one can determine the contributions arising from γ-ray, proton, and α-particle like events. An example of the fitting procedure is shown in Fig. 4, which is performed across the full energy range of Fig. 3 in bands of 128 keVee. The respective contributions are then extracted for each energy band and spectra can be constructed for each species. We identify in Fig. 4 the contributions of γ-ray, proton, and α-particle like events as those distributions with centroids at ~0.69, 0.67, and 0.64 respectively. Fig. 5 shows the resultant spectra for both fast and thermal exposures where in each separate case the contributions attributed to γ-ray, proton, and α-particle like events are plotted as a function of energy. This further clarifies the difference in response resulting from exposure to fast neutrons. The level of separation of the resulting loci is determined via a Figure of Merit (FoM) [16] which will be fully discussed in a later section.

Selecting events consistent with the γ-ray, proton and α-particle channels, Fig. 6 shows the average waveforms for events between 2 MeVee and 2.2 MeVee. From these events, one can characterise the difference in pulse decay time. The time for the pulse to decay from 90% to 10% of its maximum is, for the waveforms shown in Fig. 6, 11.34 μs, 10.16 μs and 9.20 μs for γ rays, protons and α particles, respectively. CHC is a slow scintillator, with decay times of ~2–4 μs having been reported previously when read out with a fast photomultiplier tube (PMT) [8], we conclude that the discrepancy between this and our reported decay time is due to convolution with the slower SiPM.

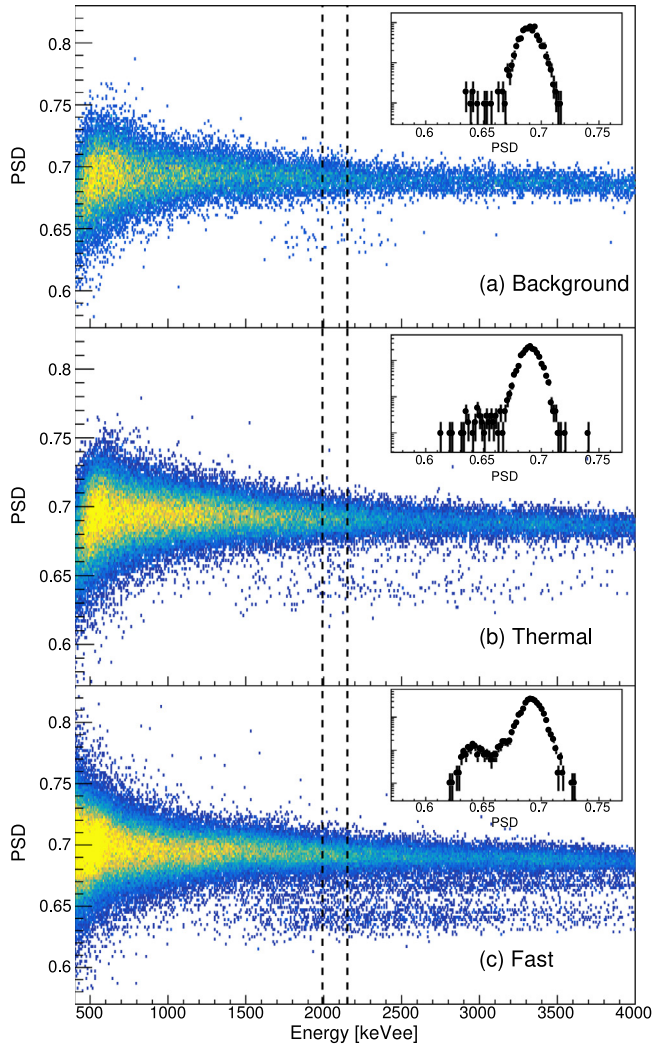

Fig. 3. Pulse-shape discrimination parameter (PSD, Eq. (1)) plotted against the γ-ray calibrated energy for the background (a), thermal (b) and fast (c) experimental configurations. There are clear excesses with two strongly populated channels in the fast configuration corresponding to the ^{35}Cl(n,p) and ^{35}Cl(n,α) reactions. The insets show projections along the PSD axis between the dashed lines for the three configurations, demonstrating the additional counts in the PSD loci. For an expanded projection along the PSD axis showing the alpha, proton and gamma ray contributions, see Fig. 4.

3. Results & discussion

The PSD shown in Fig. 3 can be quantified by a figure-of-merit (FoM) [16], indicating how well separated the different PSD loci are. The FoM is defined as

$$FoM = \frac{C(x) - C(y)}{|\Gamma(x) + \Gamma(y)|}, \tag{2}$$

where x and y correspond to the different loci (i.e. proton and α), Γ is the full width at half maximum and C is the centroid of peaks in the projection of the PSD axis. Fig. 7 shows the FoM plotted against the observed energy for CHC as calculated using the fast experimental configuration. The values for CHC here are rather similar to those determined in $LaCl_3$ [7]. A nominal limit for complete separation is an FoM of 1.26, corresponding to a separation of more than 3σ [17]. The values shown in Fig. 7 are somewhat lower, however there are some potential avenues for improvement. Most importantly, the crystal employed in the present work exhibited a resolution between 3–4 times worse than has previously been demonstrated for this material [9], likely due to imperfections inhibiting light collection. Any improvement in light collection to recover this resolution would be expected to

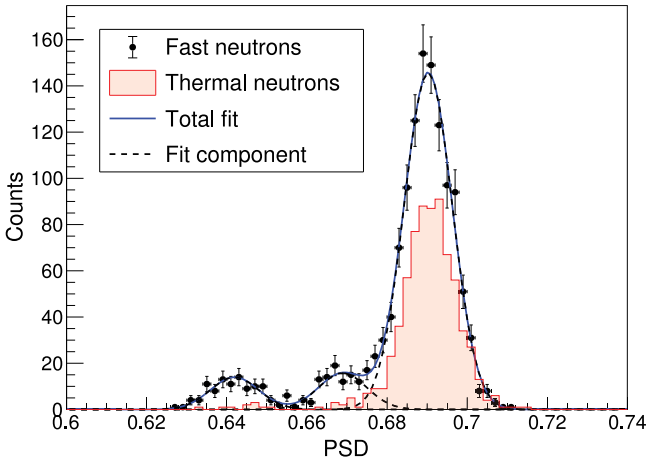

Fig. 4. A demonstration of the fitting technique used to extract spectra for proton-, α- and γ-like events. The spectrum corresponds to Fig. 3(c), projected onto the PSD axis for energies between 2684 keVee and 2812 keVee (electron-equivalent energy scale). The fit (solid blue line) is made up of three normal distributions (dashed black lines) corresponding to, from left to right, α, proton and γ-ray events. The area of each distribution is then used to determine the number of counts. Also shown (red, filled histogram) is the thermal distribution.

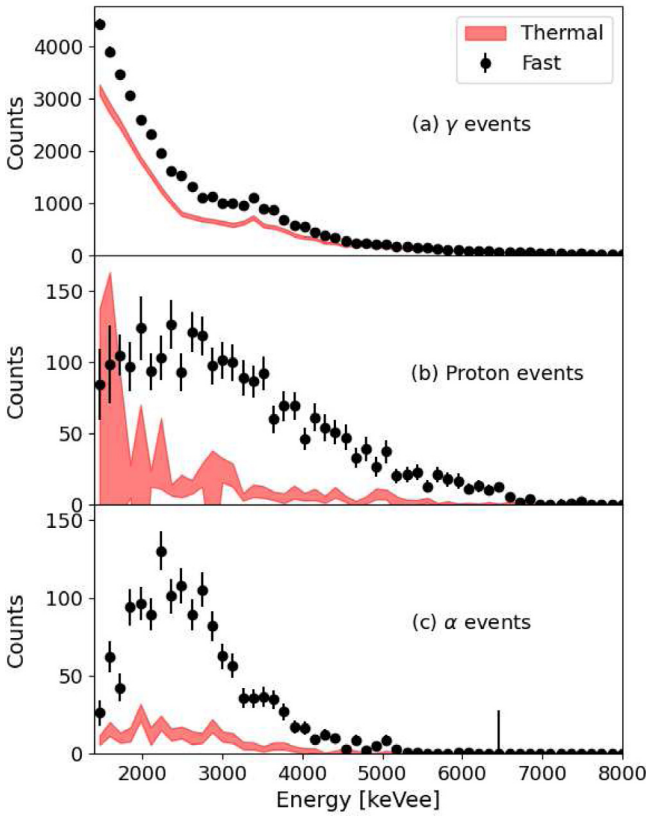

Fig. 5. Observed spectra for γ-ray (a), proton (b) and α (c) like events for the fast (black points) and thermal (red band) experimental configurations. Each point corresponds to a 128-keVee bin width. The extent of the red band indicates the $\pm 1\sigma$ uncertainties on the thermal measurement. There is a clear and significant excess in counts for the proton and α-particle like events in the fast configuration arising from the ^{35}Cl(n,p) and ^{35}Cl(n,α) reactions, while some excess is seen for the γ-rays due to the reduction in attenuation arising from the removal of the water moderation.

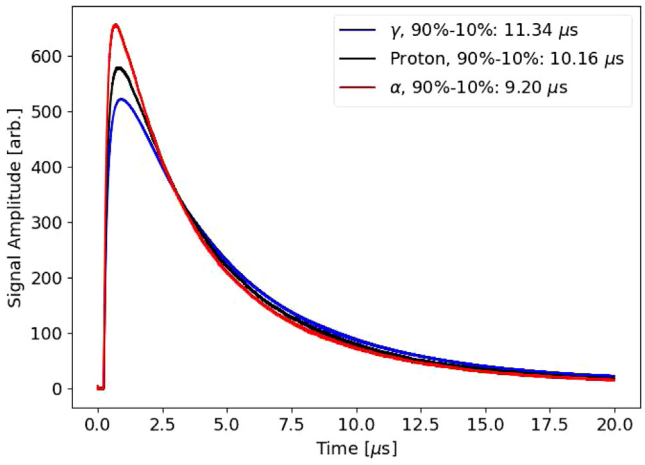

Fig. 6. Average pulse shapes from Cs_2HfCl_6 arising from γ-ray, proton and α particle events. The average pulses are calculated based on all events satisfying the associated PSD condition between 2 MeVee and 2.2 MeVee. Shown in the legend are the time taken for the averaged pulses to decay from 90% to 10% of their maximum amplitudes.

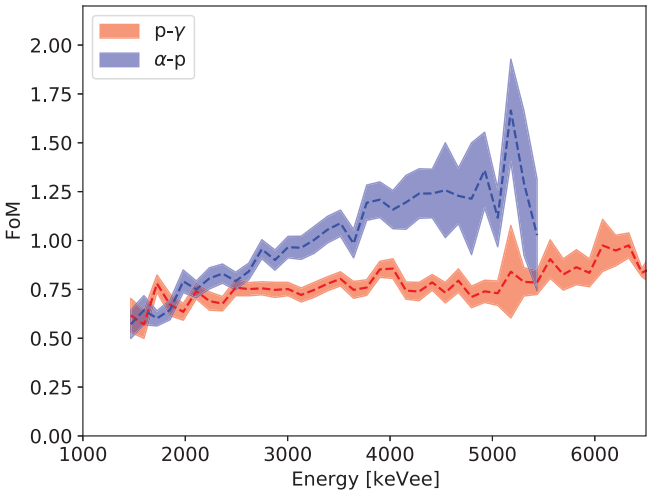

Fig. 7. Figure of merit (FoM, Eq. (2)) for Cs_2HfCl_6 for the proton and γ, and α and proton loci, plotted against the energy deposited in the crystal. Filled bands indicate the $\pm 1\sigma$ uncertainties about the central values (dashed lines).

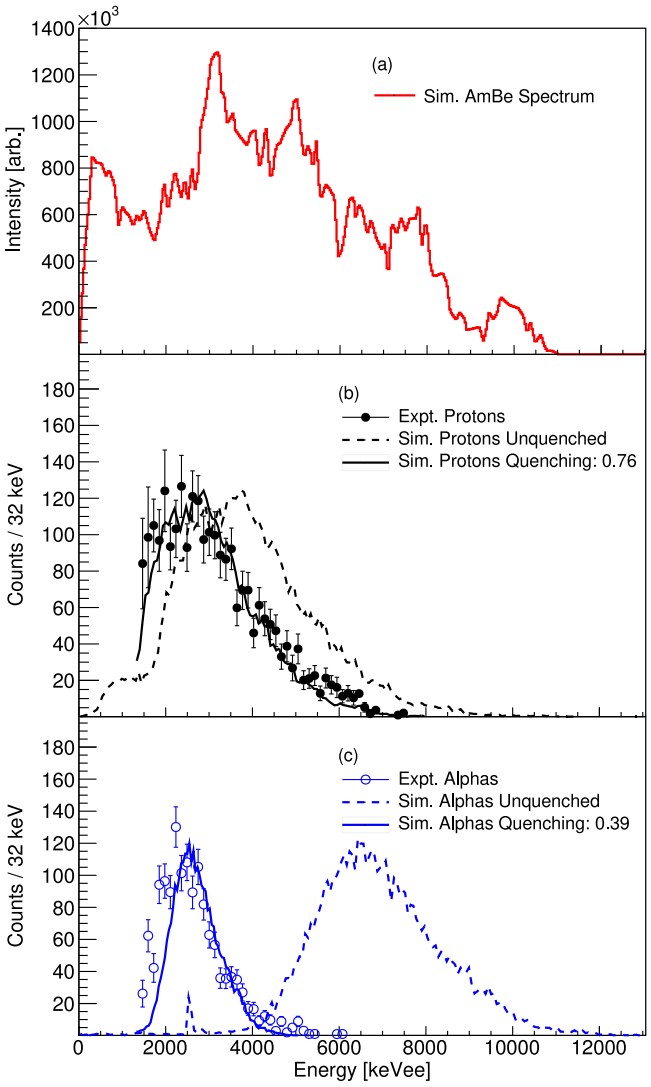

Fig. 8. (a) Simulated incident neutron spectrum. (b) Experimental (points), simulated-quenched (solid line) and simulated-unquenched (dashed line) proton deposition events. (c) as (b) but for α events. Quenchings of 0.76 and 0.39 were found for proton and α-like events, respectively.

improve the FoM by reducing variance in the waveform and narrowing the peaks in the PSD spectrum [18]. A full assay of CHC crystals and a careful optimisation of the optical setup so as to determine the best achievable FoM will be the subject of future work.

The experimental values obtained here were also compared to a Monte Carlo simulation performed using GEANT4 [19]. The simulation addresses the question of the quenching of the energy deposition spectrum and the relative efficiencies of the proton and α channels. Quenching is a well-known effect whereby α-particle and proton events result in a reduced light yield when compared to γ rays [20].

The incidence of particles with large linear energy transfer on a scintillator (i.e. α particles) causes the change in pulse shape used to perform PSD, but also results in a quenching of the energy deposition spectrum as compared to γ-ray irradiation. As the majority of detector calibrations are performed with γ-ray sources, this quenching must be corrected for in order to extract any spectroscopic information from the detection of charged particles. For example, in CLYC the thermal ^{6}Li(n,t) capture (Q = 4.8 MeV) is observed at an electron-equivalent energy of about 3.3 MeV - a quenching of 0.69 [21].

Here, we quench the simulated proton and α deposition spectra (which assume perfect energy collection) so as to best reproduce the experimentally observed spectra. Note that a single quenching parameter is used for each of the proton and α spectra, whereas in reality there may be some additional energy dependence to the quenching. The top panel of Fig. 8 shows the simulated incident neutron spectrum from the simulated AmBe source. The middle and bottom panels show the fit of the simulated spectra for protons and α particles, respectively. Also shown are the unquenched simulated spectra. Quenchings of the proton and α spectra of 0.76 and 0.39 are found, respectively.

A comparison to the simulation of the relative contributions from proton and α-like events was also made. Accounting for the thresholds in observing protons and adjusting for the fitted quenching, $p/\alpha_{(sim.)}$ = 2.07(2), whereas $p/\alpha_{(expt.)}$ = 1.78(8). This discrepancy might be explained by the slight excess in α-particle events at lower energies in the bottom panel of Fig. 8. It may also be due to some deficiencies arising from the simplified geometry employed in the simulation.

4. Conclusions

The fast-neutron response of the novel scintillator Cs_2HfCl_6 has been demonstrated for the first time. Pulse-shape discrimination was used to identify two neutron-induced reaction channels on ^{35}Cl: (n,p) and

(n,α). Importantly, when compared to $LaCl_3$ in which these channels were also recently demonstrated [7], there is no sign of significant α contamination, giving full access to the $^{35}Cl(n,\alpha)$ channel. Through comparison with Monte Carlo simulations the quenching of the proton and α particles relative to γ rays was also assessed and found to be 0.76 and 0.39, respectively.

There are potential avenues to improve the pulse-shape discrimination of the material. The selection of the photo detector was driven by prior work on developing compact, low-power neutron detectors with achieving the absolute maximum PSD and energy resolution a secondary concern. It is widely known that even with the advances in SiPM technology in recent years a traditional PMT still produces superior energy resolution [22]. The combined crystal and photodetector system used here, but parsed through an Ortec EasyMCA (multichannel analyser), provided a γ-ray resolution of 6.27(4)% at 661.64 keV compared to that reported previously of ~4% [8,11]. A study making use of different light-collection setups and careful selection of high optical-quality crystals might therefore be expected to provide an improved FoM and a full assay of crystals and photodetection methods will be the next step.

The FoM presented in this work should therefore be considered a lower-bound of what is achievable with the material. Cs_2HfCl_6 is a novel material, meaning that it is still very much under development. Tests with alternate dopants might be found to further improve the FoM beyond the 3σ limit, making the reaction channels easily accessible through a simple region-of-interest analysis.

CRediT authorship contribution statement

M.P. Taggart: Conceptualization, Investigation, Formal analysis, Writing - review & editing. **J. Henderson:** Conceptualization, Investigation, Formal analysis, Writing - original draft. **J. O'Neill:** Validation. **R. Hawrami:** Growth and preparation of scintillator samples. **E. Ariesanti:** Growth and preparation of scintillator samples. **A. Burger:** Growth and preparation of scintillator samples. **P.J. Sellin:** Resources, Writing - review & editing.

Declaration of competing interest

The authors declare that they have no known competing financial interests or personal relationships that could have appeared to influence the work reported in this paper.

Acknowledgement

The contribution of JH was supported under UKRI Future Leaders Fellowship grant no. MR/T022264/1.

References

[1] J. Glodo, W.M. Higgins, E.V.D. van Loef, K.S. Shah, IEEE Trans. Nucl. Sci. 55 (2008) 1206.
[2] T. Martinez, et al., Nucl. Instrum. Methods Phys. Res. A 906 (2018) 150–158.
[3] N. D'Olympia, P. Chowdhury, E. Jackson, C. Lister, Nucl. Instrum. Methods Phys. Res. A 763 (2014) 433–441.
[4] L.E. Kirsch, M. Devlin, S. Mosby, J. Gomez, Nucl. Instrum. Methods Phys. Res. A 874 (2017) 57–65.
[5] R. Hawrami, E. Ariesanti, L. Soundara-Pandian, J. Glodo, K.S. Shah, IEEE Trans. Nucl. Sci. 63 (2016) 2838.
[6] U. Shirwadkar, R. Hawrami, J. Glodo, E.V.D. van Loef, K.S. Shah, IEEE Nucl. Sci. Symp. Med. Imaging Conf. (2012) 1963.
[7] M.P. Taggart, J. Henderson, Nucl. Instrum. Methods A 975 (2020) 164201.
[8] A. Burger, et al., Appl. Phys. Lett. 107 (2015) 143505.
[9] E. Ariesanti, R. Hawrami, A. Burger, S. Motakef, J. Lumin. 217 (2020) 116784.
[10] T. Brown, et al., 954, 2020, 161123, http://dx.doi.org/10.1016/j.nima.2018.08.082, http://www.sciencedirect.com/science/article/pii/S0168900218310404.
[11] S. Lam, C. Guguschev, A. Burger, M. Hackett, S. Motakef, Crystal growth and scintillation performance of Cs_2HfCl_6 and $Cs_2HfCl_4Br_2$, J. Cryst. Growth 483 (2018) 121–124.
[12] R. Hawrami, E. Ariesanti, V. Buliga, L. Matei, S. Motakef, A. Burger, Advanced high-performance large diameter Cs2HfCl6 (CHC) and mixed halides scintillator, J. Cryst. Growth 533 (2020) 125473.
[13] D.A. Brown, et al., Nucl. Data Sheets 148 (2018) 1.
[14] M.P. Taggart, P.J. Sellin, Nucl. Instrum. Methods A 908 (2018) 148–154.
[15] R. Brun, F. Rademakers, Nucl. Instrum. Methods A 389 (1997) 81–86.
[16] R. Winyard, J.E. Lutkin, G.W. McBeth, Pulse shape discrimination in inorganic and organic scintillators i, Nucl. Instrum. Methods 95 (1971) 141–153.
[17] N. Zaitseva, et al., Plastic scintillators with efficient neutron/gamma pulse shape discrimination, Nucl. Instrum. Methods A 668 (2012) 88–93.
[18] M.W.J. Hubbard, Light transport modelling of pulse shape discrimination within plastic scintillators, Ph.D. thesis, University of Surrey, 2020.
[19] S. Agostinelli, et al., Nucl. Instrum. Methods Phys. Res. A 506 (2003) 250–303, http://dx.doi.org/10.1016/S0168-9002(03)01368-8, http://www.sciencedirect.com/science/article/pii/S0168900203013688.
[20] J. Birks, Theory and practice of scintillation counting, Pergamon, Oxford, United Kingdom, 1964.
[21] A. Bessiere, P. Dorenbos, C.W.E. van Eijk, K.W. Kramer, H.U. Gudel, New thermal neutron scintillators: $Cs_2LiYCl_6:Ce^{3+}$ and $Cs_2LiYBr_6:Ce^{3+}$, IEEE Trans. Nucl. Sci. 51 (5) (2004) 2970–2972.
[22] M. Grodzicka-Kobylka, M. Moszyński, T. Szczęśniak, Silicon photomultipliers in gamma spectroscopy with scintillators, Nucl. Instrum. Methods A 926 (2019) 129–147.